Research Square

Preprints are preliminary reports that have not undergone peer review.
They should not be considered conclusive, used to inform clinical practice,
or referenced by the media as validated information.

Construction of 3D Cell Spheroids Based on Chemically Modified Hyaluronic Acid Biomimetic Hydrogel for 1-Nitropyrene Toxicity Evaluation

Guojie Zhao
North China University of Science and Technology
Conghui Liu
North China University of Science and Technology
Yanlei Ge
North China University of Science and Technology
Xuemin Yao
North China University of Science and Technology
Hongjiao Wu
North China University of Science and Technology
Yishuang Cui
North China University of Science and Technology
Weinan Yao
North China University of Science and Technology
Junqing Gan
North China University of Science and Technology
Guogui Sun
guogui_sun2021@sina.com

North China University of Science and Technology

Research Article

Keywords: Hyaluronic acid, Hydrogel, Dual-network structure, Cell spheroid, 1-Nitropyrene, In vitro toxicity evaluation

Posted Date: June 19th, 2026

DOI: https://doi.org/10.21203/rs.3.rs-9934280/v1

License: This work is licensed under a Creative Commons Attribution 4.0 International License.
Read Full License

Additional Declarations: No competing interests reported.

Construction of 3D Cell Spheroids Based on Chemically Modified Hyaluronic Acid Biomimetic Hydrogel for 1-Nitropyrene Toxicity Evaluation

Guojie Zhao[1]| Conghui Liu[2]| Yanlei Ge[2,4,5,6,7]| Xuemin Yao[8]| Hongjiao Wu[2]| Yishuang Cui[8]| Weinan Yao[2]| Junqing Gan[2,7]| [*]Guogui Sun[2,3,4,5,6,7]

[1] School of Public Health, North China University of Science and Technology, Tangshan, Hebei Province, 063210, China

[2] Affiliated Hospital of North China University of Science and Technology, Tangshan, Hebei Province, 063000, China

[3] Department of Hebei Key Laboratory of Medical-Industrial Integration Precision Medicine, Tangshan, Hebei Province, 063000, China

[4] Hebei Province biological cell function development and precision detection technology Innovation Center, Tangshan, Hebei Province, 063000, China

[5] Department of Tangshan Key Laboratory of Medical-Industrial Integration Precision Medicine, Tangshan, Hebei Province, 063000, China

[6] Tangshan Biological Cell Function Development and Detection Innovation Technology Center, Tangshan, Hebei Province, 063000, China

[7] Sun Guogui Innovation Studio, Tangshan, Hebei Province, 063000, China

[8] Department of Oncology Radiation Physics Technology Section, Affiliated Hospital of North China University of Science and Technology, Tangshan, Hebei Province, 063000, China

[*]Corresponding author: guogui_sun2021@sina.com

Abstract: Air pollutants pose a severe threat to respiratory system health. Establishing an in vitro toxicological assessment model that can closely mimic the in vivo physiological state is of great significance for replacing animal experiments and improving the accuracy of toxicity prediction. Conventional two-dimensional (2D) cell culture fails to recapitulate the tissue microenvironment and pollutant concentration gradients, often resulting in deviations from the true physiological conditions in the assessment of toxicity responses. Therefore, this study was dedicated to constructing an in vitro 3D cell model suitable for the toxicity assessment of air pollutants. A thiol-cytosine dual-functional hyaluronic acid precursor (HA-SH-HMDA-Cytosine) was synthesized through chemical modification. Subsequently, a dual-network biomimetic hydrogel (Hybrid gel) was constructed through the synergistic interplay between covalent crosslinking of disulfide bonds and physical crosslinking formed by triple hydrogen bonds between cytosine and its tautomer. The obtained hydrogel possessed appropriate gelation time, porous microstructure, swelling behavior and mechanical strength. After being functional modified with RGDS peptide, the hydrogel can efficiently support the adhesion and proliferation of human bronchial epithelial BEAS-2B cells, enabling the cells to self-assembe into structurally regular lung spheroids, and its culture performance is comparable to that of Matrigel. Meanwhile, 1-nitropyrene (1-NP) was selected as a model air pollutant for toxicity assessment. The results demonstrated that the toxicity response of this lung spheroid model was more physiologically relevant than that of traditional 2D culture, accompanied by a significantly elevated IC_{50} value. Mechanistic studies revealed that 1-NP induced excessive reactive oxygen species production, triggered lipid peroxidation and cell membrane damage, and down-regulated the expression of tight junction proteins including ZO-1, Occludin and Claudin-1, thereby impairing the airway epithelial barrier function. In summary, the 3D cell culture system based on HA biomimetic hydrogel developed in this study provides a novel, stable and reliable alternative model for the in vitro toxicological assessment of air pollutants, and offers a feasible strategy for the reduction, replacement and refinement of experimental animals in accordance with the 3R principles.

Keywords: Hyaluronic acid; Hydrogel; Dual-network structure; Cell spheroid; 1-Nitropyrene; In vitro toxicity evaluation

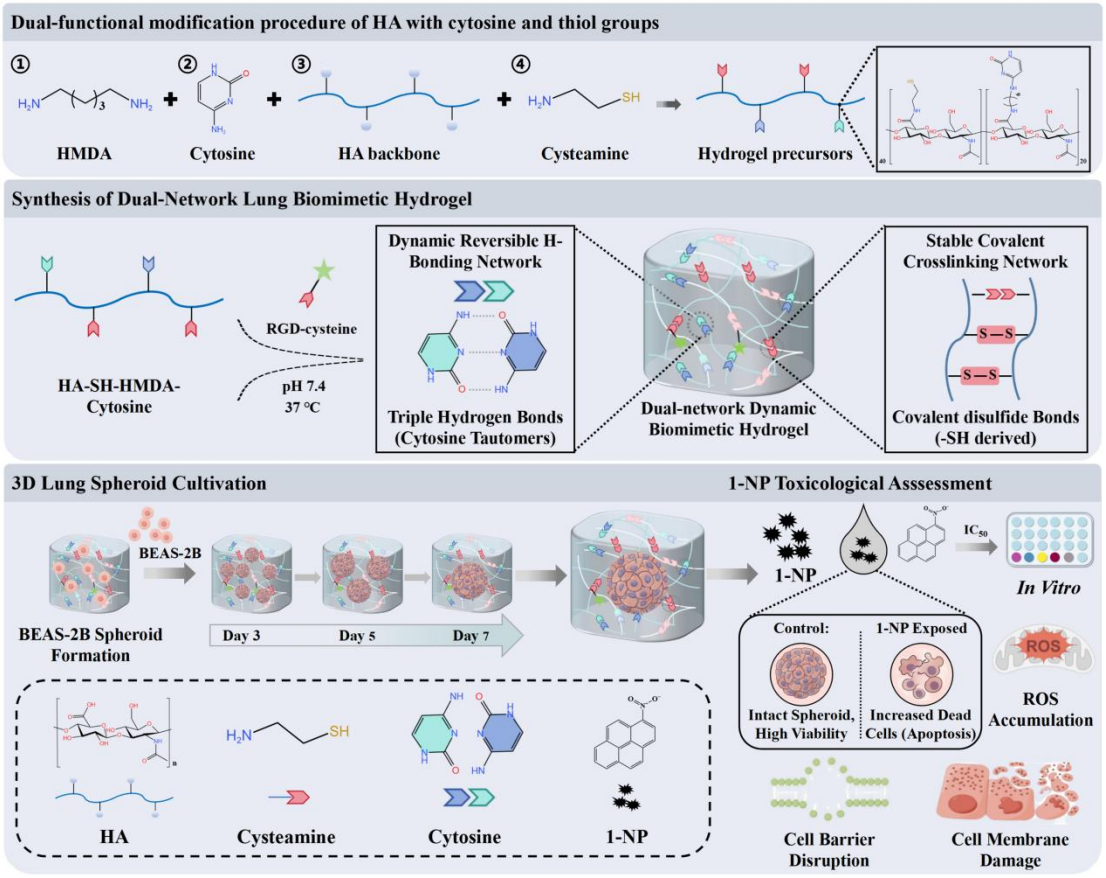
Introduction

Air pollutants mainly originate from human production activities and daily living behaviors, posing a severe threat to human health and imposing substantial disease and socioeconomic burdens. As the foundation for environmental governance, health risk assessment of environmental pollutants is of vital importance for formulating scientific and effective pollution control strategies[1,2]. For a long time, researchers have predominantly relied on animal models to assess the health risks of air pollutants, and animal models have long been regarded as the gold standard in toxicological research[3]. However, conventional animal experiments inherently have limitations such as long cycles, high costs, and significant species differences. To enhance research efficiency and reduce animal usage, an increasing number of studies have turned to in vitro testing as alternative approaches[4,5]. Although traditional two-dimensional (2D) cell culture systems enable uniform exposure of cells to contaminants, they fail to recapitulate the gradient distribution and local concentration differences of contaminants in vivo, often leading to inaccurate estimation of toxic effects, thereby causing discrepancies between in vitro results and the actual in vivo reactions[6]. In contrast, 3D cell culture system can effectively reconstruct the spatial arrangement of cells, the interaction between cells and the matrix, as well as the concentration gradients of nutrients, oxygen, and signaling molecules. By highly simulating the natural physiological microenvironment of tissues, the 3D culture technique can more accurately reflect the toxicological responses of cells and tissues to environmental pollutants, making them especially well-suited for toxicity assessments involving cell communication and epithelial barrier function[7,8].

A primary challenge in 3D cell culture is limited mass transfer efficiency[9,10]. When cells aggregate to form spheroids or organoids, the core region frequently suffers from insufficient oxygen and glucose supply, accompanied by the accumulation of metabolic wastes such as lactate and carbon dioxide, ultimately leading to cell necrosis[11,12]. As a highly hydrated advanced polymer network, 3D hydrogels are ideally suitable for meeting the physiological demands of the cellular microenvironment for 3D culture[13]. By precisely regulating the pore parameters, the novel biomimetic hydrogels can construct a micron-scale interconnected porous network, achieving efficient mass transport. Such biomimetic micro-topological structures are regarded as “breathable” scaffolds capable of autonomous substance exchange. Not only do they support efficient permeation of nutrients and oxygen (diffusion coefficient close to that of natural soft tissues), but they also facilitate the timely clearance of metabolic by-products, thereby significantly improving cell viability and growth homeostasis during long-term 3D culture[14,15]. The natural extracellular matrix (ECM) acts as both a structural scaffold for maintaining cell morphology and a critical biochemical and mechanical regulatory factor for cell functions[16]. As an essential component of the ECM, hyaluronic acid (HA) has been widely utilized in the design of engineered hydrogels owing to its inherent biological functions and abundant modifiable sites[17]. Nevertheless, natural HA is compromised by poor mechanical properties and rapid degradation in vivo, which severely restrict its practical applications and necessitate structural optimization through chemical

modification[18]. In recent years, to enhance the mechanical strength and biological activity of HA hydrogels, researchers have optimized their performance by constructing sophisticated cross-linking structures or introducing efficient energy dissipation mechanisms[19].

In this study, a dual-network dynamic biomimetic hydrogel based on HA was designed and fabricated, aiming to establish a 3D lung spheroid model derived from the human bronchial epithelial cell line BEAS-2B. To construct a reversible dynamic hydrogen-bonding network, cytosine was selected as the modifying molecule for HA. This nucleobase is capable of forming triple hydrogen bonds with its tautomer under physiological pH conditions[20]. However, previous studies have confirmed that directly modifying HA with cytosine fails to yield nucleobase-functionalized HA hydrogels. This phenomenon is mainly attributed to the low grafting rate, as well as the severe steric hindrance caused by the lack of long spacer linkers between the HA chains and cytosine moieties[21]. Therefore, to improve the grafting efficiency of cytosine and effectively alleviate molecular steric hindrance, 1,6-hexamethylenediamine (HMDA) was employed as a long-chain bridging unit to synthesize the hyaluronic acid-hexamethylenediamine-cytosine derivative (HA-HMDA-Cytosine). To construct a stable covalent crosslinking network, sulfhydryl groups (-SH) were further introduced into the molecular backbone of HA-HMDA-Cytosine to prepare its thiolated derivatives (HA-SH-HMDA-Cytosine), which provided abundant active sites for the subsequent covalent crosslinking of the hydrogel. Covalent crosslinking can optimize the solid content of the hydrogel and enhance its structural stability, thereby avoiding undesirable degradation during cell culture[22]. By adjusting the weight/volume percentage (w/v) of HA in the system, the crosslinking density of the hydrogel can be precisely modulated, enabling its mechanical properties to be tailored to match the physiological microenvironment of lung tissues.. Meanwhile, Arg-Gly-Asp-Cys (RGDS) adhesive peptide was incorporated into the gel network to further optimize the biological activity and cell adhesion performance of the scaffold[23]. Based on this, the effects of hydrogels with different crosslinking densities and crosslinking modes on the adhesion, spreading and proliferation of BEAS-2B cells were systematically investigated. Subsequently, a 3D lung spheroid model derived from the BEAS-2B cell line was constructed using the dual-network biomimetic hydrogel. Finally, 1-nitropyrene (1-NP), a typical atmospheric pollutant, was selected for exposure assessment to validate the application potential of the 3D spheroid model in the toxicological evaluation of air pollutants (Scheme 1). In summary, this study successfully developed a biomimetic hydrogel material suitable for 3D cell culture. As an innovative in vitro modeling platform, the prepared material provides a reliable system for the toxicity assessment of air pollutants and related fundamental research, and holds great potential for reducing and even replacing the use of experimental animals.



Scheme 1. Schematic diagram of the construction of BEAS-2B lung cell spheroids based on dual-network HA hydrogels and their application as a model for toxicity assessment of environmental pollutants.

2 Material and Methods

2.1. Chemicals and Materials

Low-molecular-weight sodium hyaluronate (Molecular weight: 200~400 kDa, cosmetic grade), L-cysteine hydrochloride (molecular weight: 157.62 Da, purity ≥ 98%), 1-(3-dimethylaminopropyl)-3-ethylcarbodiimide hydrochloride (EDC, molecular weight: 191.70 Da, purity ≥ 98%), N-hydroxysuccinimide (NHS, molecular weight: 115.09 Da, purity ≥ 98%), 1,6-hexanediamine (HMDA, molecular weight: 116.2 Da, purity ≥ 99%), cytosine (molecular weight: 111.1 Da, purity ≥ 98%), and hydroquinone (molecular weight: 110.11 Da, purity ≥ 98%) were purchased from Shanghai Aladdin Biochemical Technology Co., Ltd., China. Dialysis bags MD25 with molecular weight cut-off (MWCO) of 3500 Da and 10000 Da were obtained from Beijing Solarbio Science & Technology Co., Ltd., China. Deuterium oxide (D_2O) was supplied by Adamas Reagent Co., Ltd., China. RGDS peptide was purchased from Shanghai ACMEC Biochemical Technology Co., Ltd., China. The human lung epithelial cell line BEAS-2B was preserved in the cell bank of our laboratory. All the other reagents used in this study were of analytical purity and commercially available.

2.2. Synthesis of HA-based hydrogel precursor

HA-SH-HMDA-Cytosine was synthesized through a three-step route involving transamination and amidation reactions, with the detailed procedures performed

according to reported literature[24-26]. Firstly, the hydrophobic linker Cytosine-HMDA was synthesized through transamination reaction. Subsequently, HA-HMDA-Cytosine was prepared through the amidation reaction. Finally, another amidation reaction was conducted to yield the target product HA-SH-HMDA-Cytosine. Detailed synthetic protocols and reaction parameters can be found in the supplementary materials. Fourier transform infrared spectroscopy (FTIR) and proton nuclear magnetic resonance spectroscopy (^{1}H NMR) were used to characterize the chemical structures of the hydrogel precursors. The corresponding spectral results are displayed in Supplementary Figure 2 and Supplementary Figure 3.

2.3. Preparation of HA-Based Hydrogel

In this study, the concentrations of HA-based hydrogels were expressed as weight/volume percentage (% w/v), and the density of HA was 1.78 g·mL^{-1}. To mimic the 3D cell culture microenvironment, PBS (pH 7.4) was used as the solvent. HA-SH-HMDA-Cytosine macromonomers were separately prepared into solutions of 1.5%, 2.0% and 2.5% (w/v). Gelation was performed under physiological conditions at 37 °C and pH 7.4 to fabricate dual-network hybrid hydrogels (Hybrid gels). For comparison, HA-SH covalently crosslinked hydrogels (Covalent gels) were also fabricated by preparing HA-SH solutions at the same w/v concentrations in the identical solvent system. Each group of hydrogel precursor solutions was transferred into 1.5 mL centrifuge tubes. The gelation time was determined by the tube inversion method, which was defined as the point when the solution stopped flowing.

2.4. Characterization

2.4.1 ^{1}H NMR

^{1}H NMR spectra were recorded on a nuclear magnetic resonance spectrometer (Avance 400, Bruker Ltd., Germany). A suitable amount of lyophilized hydrogel precursor samples was dissolved in D_2O to prepare a concentration of 10 mg/mL, and then subjected to spectral acquisition for ^{1}H NMR measurement.

2.4.2 FTIR

Approximately 1~2 mg of lyophilized samples was fully ground and mixed with 200 mg of potassium bromide (P116273, Aladdin, China) powder in an agate mortar, followed by tablet pressing. The samples were scanned with a Fourier transform infrared spectrometer (Nicolet-5700, Thermo Ltd., USA), and the corresponding infrared spectra were recorded.

2.4.3 Swelling test

The masses of hydrogel samples in the dry state and at swelling equilibrium were weighed separately. The swelling ratio of the hydrogel was calculated according to Formula (2-1), where W_0 and W_1 represent the mass of the hydrogel in the dry state and swollen state, respectively.

$$\text{Swelling rate (\%)} = \frac{W_1 - W_0}{W_0} \times 100 \quad (2\text{-}1)$$

2.4.4 scanning electron microscopy (SEM)

The porous microstructure of hydrogel samples was observed by SEM (TM-1000, Hitachi Ltd., Japan). Lyophilized hydrogel specimens were quenched and fractured in liquid nitrogen, followed by gold sputtering. SEM images were performed at an

accelerating voltage of 15 kV.

2.4.5 Rheology

A rotational rheometer (Kinexus Ultra+, NETZSCH, Germany) was used to perform frequency sweep tests at 25 °C (Strain: 5%, Frequency: 0.1–10 Hz). The storage modulus (G') and loss modulus (G'') were determined to evaluate the mechanical strength and network structural stability of the hydrogels.

2.5 Cell culture

2.5.1 Cell adhesion

BEAS-2B cells were seeded onto the surface of sterilized hydrogels at a density of 2.5×10^4 cells/cm². Each well was added with 1 mL of DMEM medium (03.1006C, allBio, China) supplemented with 10% fetal bovine serum (164210, Procell, China) and 1% penicillin–streptomycin (C100C5, NCM Biotech, China). The cells were cultured at 37 °C in a 5% CO_2 incubator (HCP-168E, Haier Biomedical, China) for 6 h. Subsequently, cells were stained with Calcein-AM (KGA9501, KEYGEN BIOTECH, China) for live cell fluorescent labeling. Fluorescent imaging was performed using an inverted laser scanning confocal microscope (LSM 900, Carl Zeiss AG, Germany), and the all imaging procedures were controlled by ZEISS ZEN 3.7 software.

2.5.2 Cell proliferation

BEAS-2B cells were seeded onto sterile hydrogel surfaces at a density of 1×10^4 cells/cm² and cultured in an incubator in a 5% CO_2 at 37 °C for 1, 3, and 5 days, respectively. After incubation with CCK-8 working solution (K1018, Affinity Biosciences, China) for 2 h, the absorbance at 450 nm was measured using a microplate reader (Multiskan FC, Thermo Scientific, USA). The obtained absorbance data were recorded and analyzed to evaluate cell proliferation activity.

2.6 Construction of BEAS-2B 3D spheroids based on HA-based hydrogels

BEAS-2B cells were seeded into the HA-based hydrogel scaffolds at a density of 5×10^4 cells/cm² and cultured in a constant-temperature incubator at 37 °C with 5% CO_2 for 1, 3, 5, and 7 days, respectively. The proliferation activity of cell spheroids was detected using the CCK-8 assay, and spheroid diameters were quantitatively analyzed using Image J software (version 1.54r). At room temperature in the dark, the cytoskeleton and cell nuclei were separately stained with TRITC-phalloidin (AC10878, ACMEC, China) and DAPI fluorescent dye (SL7100, Coolaber, China). The structural formation and growth process of BEAS-2B lung spheroids were observed using a laser scanning confocal microscope.

2.7 1-NP exposure treatment of 3D lung spheroids

After routine culture for 7 days, the 3D spheroids were gently rinsed three times with PBS. The medium was replaced with fresh culture medium containing different concentrations of 1-NP (0, 1, 2.5, 5, 10, 25, 50, 100, 200 and 400 μM), followed by continuous 1-NP exposure for 48 h. Morphological changes of the 3D lung spheroids were observed under bright field with an inverted microscope (ECLIPSE Ts2, Nikon, Japan). Afterwards, CCK-8 reagent was added and incubated at 37 °C for 2 h. The absorbance at 450 nm was measured with a microplate reader, and the cell viability was calculated according to Formula (2-2). Herein, Ic represents the absorbance of the

untreated control group, Is represents that of the 1-NP-treated group, and Ib indicates the absorbance of the blank control group.

$$\text{Cell viability (\%)} = \frac{I_s - I_b}{I_c - I_b} \times 100 \quad (2\text{-}2)$$

2.8 Live/Dead staining

Working solutions of Calcein-AM and propidium iodide (PI, KGA9501, KEYGEN BIOTECH, China) were prepared in accordance with the manufacturer's instructions. The 3D lung spheroids were dissociated and incubated in the staining working solution at 37 °C for 15 min in the dark, followed by three washes with PBS to remove residual dye. Fluorescence images were performed using a laser scanning confocal microscope. The fluorescence intensities of green signals (live cells) and red signals (dead cells) were quantitatively analyzed with Image J software. Cell viability was calculated as the ratio of the live cell fluorescence intensity to the total cellular fluorescence intensity.

2.9 Reactive oxygen species (ROS) detection

After exposure for 1-NP, intracellular ROS levels in 3D lung spheroids were detected using 2',7'-dichlorofluorescein diacetate (DCFDA, KGA7308, KEYGEN BIOTECH, China). DCFDA working solution was diluted to a final concentration of 10 μM. The spheroids were incubated at 37 °C for 40 min in the dark, followed by three washes with PBS to remove residual working solution. Fluorescence images were subsequently performed using a laser scanning confocal microscope. The fluorescence intensity was quantitatively analyzed using Image J software to evaluate the relative ROS levels in the spheroids.

2.10 LDH and MDA determination

The release level of lactate dehydrogenase (LDH) can directly reflect the degree of cell membrane damage and cellular necrosis. In this study, a commercial LDH assay kit (M1030, Beyotime, China) was used to determine LDH activity. After 1-NP exposure, 50 μL of cell culture supernatant was collected and mixed with an equal volume of working reaction solution, followed by incubation at room temperature for 15 min. After incubation, the absorbance was measured at 490 nm with a reference wavelength of 630 nm using a microplate reader.

Malondialdehyde (MDA), as a terminal product of lipid peroxidation, can effectively reflect cellular oxidative stress status and the degree of cell membrane damage. A commercial assay kit (AKFA013M, Boxbio, China) was used to detect MDA content based on the thiobarbituric acid (TBA) method. The supernatant of cell lysates was mixed with an equal volume of MDA working solution, and the resulting mixture was heated in a boiling water bath for 15 min. The absorbance was measured at 532 nm with a reference wavelength set at 450 nm using a microplate reader.

2.11 Western blotting

Total protein was extracted from 1-NP-exposed 3D lung spheroids using RIPA lysis buffer (P0013, Beyotime, China). Protein concentration was quantified using a BCA protein assay kit (WB6501, NCM Biotech, China). Protein samples were separated by 10% SDS-PAGE gel electrophoresis (WB2102, BIOTIDES, China) and then transferred onto PVDF membranes (IPVH00010, HKHCBIO, China). The

membranes were blocked with 5% skim milk diluted in TBST buffer (PS103S, EpiZyme, China) containing 0.5% Tween-20 at room temperature for 2 h. After removal of the blocking solution, the membranes were incubated with primary antibodies overnight at 4 °C (detailed information on primary antibodies is listed in Supplementary Table 1). Following thorough washing with TBST, the membranes were incubated with secondary antibodies diluted at a ratio of 1:10000 for 1 h at room temperature. Subsequently, ECL chemiluminescence substrate (P1050, APPLYGEN, China) was added for signal development. Protein band images were visualized using a gel imaging system (C300, Azure Biosystems, USA), and the gray values of the bands were quantitatively analyzed by Image J software.

2.12 RNA extraction and quantitative real-time PCR

Total RNA was extracted from 1-NP-exposed 3D lung spheroids using a rapid RNA extraction kit (M5105, NCM Biotech, China). The concentration and purity of RNA were determined with a microvolume spectrophotometer (NanoDrop One, Thermo Scientific, USA). Total mRNA was reverse-transcribed into cDNA using a reverse transcription kit with genomic DNA elimination enzyme (RR036A, TAKARA, Japan). Gene amplification and quantification were performed on a real-time fluorescent quantitative PCR instrument (QuantStudio 7 Flex, Applied Biosystems, USA) using 2× Universal SYBR Green Fast qPCR Mix (RR820A, TAKARA, Japan). Detailed primer sequences are listed in Supplementary Table 2.

2.13 Statistical analysis

All statistical analyses were conducted using GraphPad Prism v.8.0.1. Detailed information on statistical methods and P-values is provided in the figure legends.

3 Results and discussion

3.1 Synthesis and characterization of hydrogel precursors

The hydrogel precursor HA-SH-HMDA-Cytosine was synthesized via a three-step sequential synthetic route involving transamination and amidation reactions (Figure 1A). The detailed synthetic procedures were described as follows. Firstly, the hydrophobic linker HMDA-Cytosine was synthesized. Subsequently, it was covalently conjugated to HA chains to yield the HA-HMDA-Cytosine intermediate. Finally, further thiolation modification was performed to successfully prepare the target product HA-SH-HMDA-Cytosine. The synthetic routes and structural characterization data are presented in Supplementary Figure 1~3. Quantitative analysis based on ^{1}H NMR spectra revealed that the amidation grafting efficiency of HA-HMDA-Cytosine was approximately 19% (Supplementary Figure 3B). Meanwhile, to construct single-network covalent hydrogels independent of hydrogen bonding and solely relying on covalent crosslinking (Covalent gels), the monothiol-modified hydrogel precursor HA-SH was synchronously synthesized in this study. Its amidation modification efficiency was calculated to be about 50% according to ^{1}H NMR spectra (Supplementary Figure 3D). FTIR spectra confirmed that characteristic stretching vibration absorption peaks of the ketone carbonyl group (C=O) derived from cytosine structural units (Figure 1B) and thiol functional units (Figure 1C) were detected at 1730 cm^{-1} and 1720 cm^{-1}, respectively. After hydrogel crosslinking and formation, the intensities of these two carbonyl characteristic peaks

decreased significantly or even nearly vanished. This phenomenon indicated that intermolecular hydrogen bonds were effectively formed between ketone carbonyl and amino groups in the system, while thiol groups were oxidized to form covalent disulfide bonds[21,26]. The synergistic combination of non-covalent hydrogen bonding interactions and covalent disulfide crosslinking provides a solid molecular structural foundation for the construction of the dual-network hybrid hydrogel system.

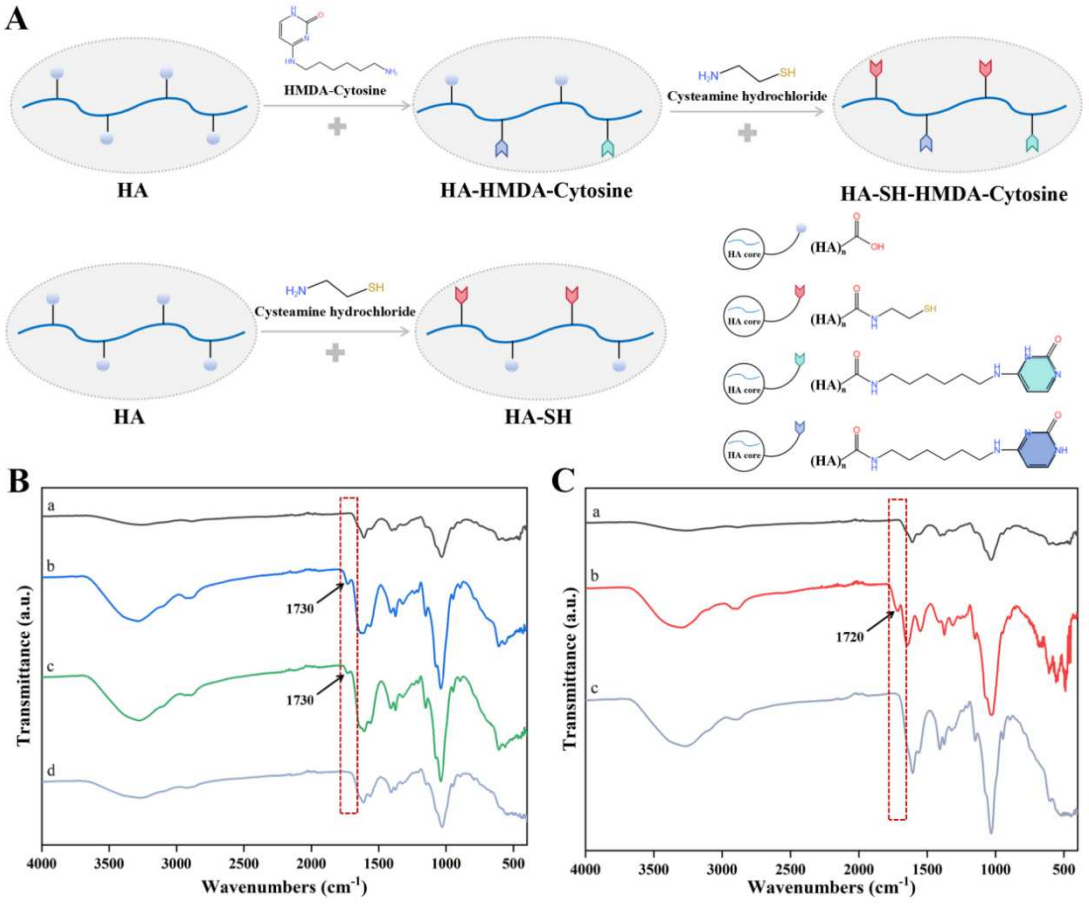


Figure 1. Design and synthesis of HA-based hydrogel precursors. (A) Schematic illustration of the synthetic route for preparing functionalized HA-based hydrogel precursors via stepwise chemical modification using HA as the starting substrate, achieving dual-group co-modification with cytosine and thiol groups. (B) FTIR spectra of HA (a), HA-HMDA-Cytosine (b), HA-SH-HMDA-Cytosine (c), and HA-HMDA-Cytosine hydrogel (d). (C) FTIR spectra of HA (a), HA-SH (b), and HA-SH hydrogel (c).

3.2 Synthesis and physicochemical properties of HA-base hydrogels

In this study, dual-network hybrid HA hydrogels (denoted as Hybrid gels) were rationally designed and fabricated. These hydrogels possess a dual crosslinking structure: one is a covalent crosslinking network formed by disulfide bonds generated via the oxidation of thiol groups[27], and the other is a physical crosslinked network constructed through triple hydrogen bonding interactions between cytosine and its tautomer[28]. HA inherently lacks cellular integrin-binding sites and exhibits extremely low protein adsorption capacity. Nevertheless, covalent conjugation of RGD cell-adhesive peptides to HA chains can effectively facilitate cell adhesion(Figure 2A)[29]. Both Covalent gels and Hybrid gels undergo rapid sol-gel transition at 37 °C

under physiological neutral pH that mimics the in vivo microenvironment, and their gelation kinetics are strongly dependent on HA concentration. At an HA mass concentration of 4.0% (w/v), the gelation time of Hybrid gels is only 2.00 ± 0.44 min; when the concentration decreases to 1.0% (w/v), the gelation time is remarkably extended to 30.67 ± 1.17 min. At the same HA concentration, Hybrid gels display distinctly shorter gelation times than Covalent gels, and such discrepancy is more pronounced at low concentrations. This indicates that intermolecular hydrogen bonding of cytosine can synergistically facilitate network crosslinking process (Figure 2B). Gelation time is a key parameter for 3D cell culture. During cell seeding and 3D culture, an excessively fast gelation rate leads to premature solidification of the hydrogel precursor solution prior to homogeneous cell mixing and spreading, thereby impeding uniform cell distribution. Conversely, an overly slow gelation rate causes cell sedimentation and aggregation, resulting in uneven cell distribution and failure to maintain normal 3D growth behaviors and morphological characteristics[30]. It is generally accepted that a gelation time of 5~20 min is optimal for 3D cell encapsulation and culture[31].

The micromorphology of the prepared hydrogels was further characterized by SEM. Both Covalent gels and Hybrid gels displayed interconnected, uniformly distributed and loose porous architectures, with pore sizes ranging from 100 to 200 μm. At the same concentration, the average pore size of Hybrid gels was obviously smaller than that of Covalent gels. This difference originates from the higher overall crosslinking density of Hybrid gels constructed by dual-network crosslinking, which thereby endows them with a denser porous microstructure (Figure 1C). Appropriate and homogeneous porous structure can effectively facilitate the diffusion and mass exchange of nutrients, oxygen and metabolic wastes within hydrogel scaffolds. Such favorable structural features are conducive to long-term 3D cell culture, maintain the viability and proliferation of encapsulated cells, and effectively alleviate central necrosis of cell spheroids caused by insufficient mass exchange[32]. Moreover, the pore size in the range of 100~200 μm not only provides sufficient spatial support for cell aggregation and 3D structural growth, but also maintains the structural stability of hydrogel scaffolds. It avoids cell crowding and compression caused by overly small pores, as well as cell shedding and loss induced by excessively large pores[33]. This structural distinction was further verified by swelling tests. All hydrogels exhibited excellent water absorption and swelling properties. At the same HA concentration, Covalent gels possessed a significantly higher equilibrium swelling ratio than Hybrid gels, further confirming that dual-network crosslinking effectively increases the crosslinking density of Hybrid gels (Figure 1D).

To evaluate the mechanical properties of the hydrogels, rheological tests were conducted on Covalent gels and Hybrid gels with different precursor concentrations under neutral pH conditions (Figure 2E and Supplementary Figure 4A, 4B). The results demonstrated that Hybrid gels possessed significantly higher storage modulus and structural stiffness than Covalent gels at all tested HA concentrations. This is primarily attributed to the synergistic crosslinking between covalent bonds and hydrogen bonds within the dual-network hybrid system, which endows the hydrogels

with elevated network crosslinking density and mechanical strength. Consistent with expectations, the equilibrium swelling behavior of hydrogels with different concentrations was dependent on solid content and negatively correlated with structural stiffness (Figure 1D). To further visually evaluate their compression resistance, a static compression test with a 50 g weight was performed (Supplementary Figure 5). Under neutral pH conditions, Covalent gels of different concentrations exhibited irreversible structural collapse after 10 min of compression. By contrast, Hybrid gels only underwent slight deformation under the same load and maintained complete structural integrity after weight removal. This phenomenon reveals that the synergistic effect of covalent crosslinking and hydrogen-bond-mediated physical crosslinking in the dual-network structure of Hybrid gels markedly enhances compressive toughness and structural stability, while effectively overcoming the brittle fracture limitation of single covalent crosslinked networks[34]. In conclusion, we successfully developed a dual-network Hybrid gel system with combined covalent crosslinking and hydrogen-bond physical crosslinking. By adjusting the concentration of HA hydrogel precursors, gelation kinetics, microscopic pore structure, swelling characteristics and mechanical properties can be precisely regulated. This hydrogel system serves as an ideal biomimetic scaffold for the subsequent establishment of 3D airway epithelial cell spheroids.

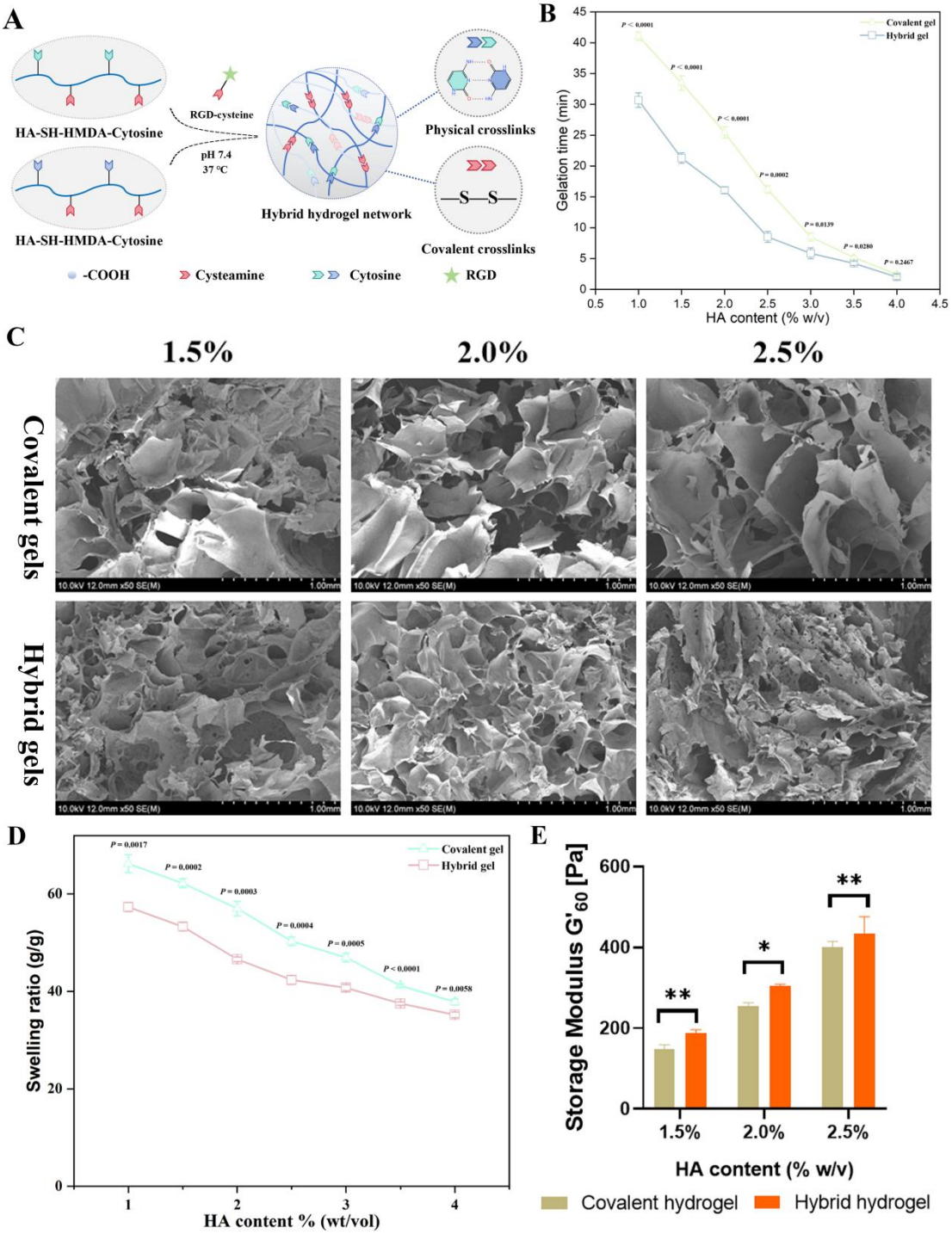


Figure 2. Synthesis and physicochemical characterization of HA-based hydrogels. (A) Schematic illustration of the copolymerization reaction of HA-SH-HMDA-Cytosine macromonomers. The system simultaneously constructs a dual crosslinking network: a covalent crosslinking network formed by disulfide bonds via thiol oxidation, and a physical crosslinking network formed via intermolecular hydrogen bonding between cytosine molecules. (B) Gelation kinetic curves of Covalent gels and Hybrid gels with different HA precursor contents (% w/v). (C) Representative SEM images of the microscopic porous structure of lyophilized hydrogels. (D) Equilibrium mass swelling ratio of Covalent gels and Hybrid gels. (E) Effects of different HA precursor contents (% w/v) on the mechanical properties of hydrogels, characterized by the elastic

modulus (G′) measured via frequency sweep at 5% strain. Data are expressed as mean ± SD (n = 3). Statistical analysis was performed via one-way analysis of variance (ANOVA) followed by Dunnett's post-hoc test. *P<0.05, **P<0.01.

3.3 Cell adhesion and proliferation on hydrogel surfaces

Cell adhesion is a pivotal event governing cell fate and modulates a series of core biological processes such as cell proliferation, migration, and differentiation[35]. However, native HA lacks specific cell adhesion sites and tends to inhibit protein adsorption, thereby resulting in insufficient cell adhesion capacity. To address this limitation, 0.5 mM RGD peptide was introduced to functionally modify the hydrogel system and optimize the cell adhesion microenvironment[23]. The promoting effects of Covalent gels and Hybrid gels with different concentrations on the adhesion and proliferation behaviors of BEAS-2B cells were systematically compared. First, Live/Dead fluorescence staining was performed to assess the viability of BEAS-2B cells cultured on Covalent gels and Hybrid gels at concentrations of 1.5%, 2.0%, and 2.5% (w/v) (Figure 3A). The results revealed that both hydrogel systems exhibited favorable biocompatibility without apparent cytotoxicity, and the cultured cells maintained high overall viability. At the same concentration, the cell density in the Hybrid gels group was markedly higher than that in the Covalent gels group, with more evident cell aggregation occurred at 1.5% and 2.0% (w/v). These findings indicated that dual-network Hybrid gels were more favorable for cell adhesion, attachment, and early colonization. Furthermore, the CCK-8 assay was applied to continuously quantify cell proliferative activity over 5 consecutive days (Figure 3B–D). The results demonstrated that both hydrogels could support the normal proliferation of BEAS-2B cells in a time-dependent pattern. On day 1 of culture, no significant difference in cell proliferation level was detected among all groups. On day 3, the cell proliferation level in the Hybrid gel group began to exceed that of Covalent gels at the same concentration. By day 5, the proliferative superiority of the 2.0% (w/v) Hybrid gel group became more prominent. In addition, 2.0% (w/v) Hybrid gels exhibited the optimal capacity to support cell proliferation at all detected time points. When the concentration was elevated to 2.5% (w/v), cell proliferation was partially suppressed in both hydrogel systems. Taken together, the above results demonstrate that dual-network Hybrid gels can provide superior cell-adhesive sites and a favorable mechanical microenvironment, effectively facilitating the adhesion, aggregation, and proliferation of BEAS-2B cells. Accordingly, 2.0% (w/v) was identified as the optimal matrix concentration for supporting cell growth and proliferation.

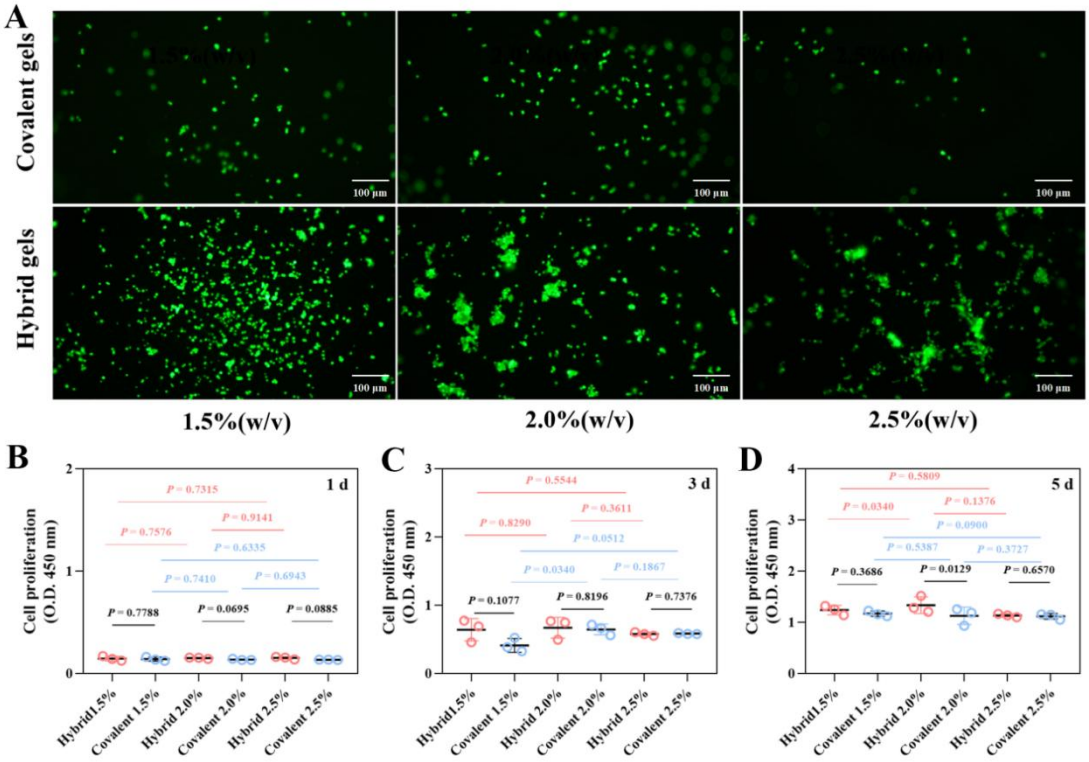


Figure 3. Effects of HA-based hydrogels on the cell **adhesion and proliferation of BEAS-2B cells.** (A) Live/Dead fluorescent staining images of BEAS-2B cells cultured on Covalent gels and Hybrid gels for 6 h of incubation(Scale bar: 100 μm). (B–D) Quantitative analysis of proliferative activity of BEAS-2B cells cultured on hydrogel scaffolds with different concentrations for 1 day (B), 3 days (C), and 5 days (D), respectively. Data are expressed as mean ± SD (*n*=3). Statistical analysis was performed via one-way ANOVA followed by Dunnett's post-hoc test.

3.4 Construction of BEAS-2B cell-derived lung spheroid model

BEAS-2B, a normal human bronchial epithelial cell line, can stably maintain the inherent physiological characteristics of the airway epithelium. It possesses favorable in vitro proliferative capacity and 3D self-assembly potential, and is highly sensitive to atmospheric pollutants, inflammatory stimuli, and pharmacological interventions. Accordingly, BEAS-2B cells have been widely used in respiratory toxicology research and investigations into the mechanisms of airway epithelial injury and repair[36]. To verify the capacity of HA-based hydrogels to support the 3D culture of BEAS-2B cells, a biomimetic 3D culture microenvironment was established in this study. BEAS-2B single cells were seeded into three different matrices, namely Matrigel, Covalent gel, and Hybrid gel, and cultured continuously for 7 days. The regulatory effects of different matrices on cell proliferation and 3D spheroid formation were systematically evaluated (Figure 4A). The establishment of a parallel culture system with multiple matrices provides experimental support and a theoretical basis for screening biomimetic scaffolds suitable for 3D spheroid construction[37]. During the culture period, Observations showed that BEAS-2B cells in Matrigel gradually aggregated over time, forming uniformly sized and well-organized spheroids. In Covalent gels, cells aggregated slowly, resulting in fewer and smaller spheroids with relatively poor overall growth viability. By contrast, distinct spheroid

structures were observed in Hybrid gels as early as day 3 of culture. By day 7, the number of spheroids increased markedly with more regular morphology, and their growth state closely resembled that in Matrigel (Figure 4B). Proliferation results indicated that cell viability in all groups increased in a time-dependent manner. On day 1, there were no significant differences in cell proliferative activity among the three groups. Starting from day 3, the proliferative activity in the Hybrid gel group was significantly higher than that in the Covalent gel group ($P<0.05$) and gradually approached the level of the Matrigel group. On day 7, there was no statistical difference in proliferation activity between the Hybrid gel and Matrigel groups, while the Covalent gel group remained significantly lower than the other two groups ($P<0.05$). These results demonstrate that Hybrid gels can effectively support the long-term proliferation of BEAS-2B cells, with culture performance comparable to that of Matrigel (Figure 4C). Statistical analysis of spheroid diameters further confirmed the above trend. On day 3, the spheroid diameter in the Hybrid gel group was significantly larger than that in the Covalent gel group ($P<0.05$) and showed no obvious difference compared with the Matrigel group. From day 5 to day 7, the spheroid diameter in the Hybrid gel group continued to increase, and the gap with the Matrigel group gradually narrowed. In contrast, spheroids in the Covalent gel group remained small throughout the culture period, with a slow growth rate (Figure 4D). Therefore, compared with single covalently crosslinked hydrogels, covalent-hydrogen bonded dual-network hydrogels exhibit a more favorable porous structure, tunable stiffness, excellent toughness, and dynamic reversibility through the synergistic effects of chemical covalent bonds and physical hydrogen bonds, thereby better mimicking the biomimetic microenvironment of the natural ECM. Cytoskeleton staining revealed that on day 3, BEAS-2B cells within Hybrid gel showed obvious cell aggregation and initial spheroid formation, with F-actin distributed in a radial pattern. By day 7, an intact cytoskeletal network had formed inside the spheroids; F-actin presented a regular circular distribution, nuclei were arranged uniformly and orderly, and the spheroid diameter reached approximately 100 μm, indicating that the cells had successfully assembled into mature, polarized epithelial-like spheroid structures (Figure 4E)[38]. In conclusion, RGD-functionalized Hybrid gels remarkably enhance cell adhesion and provides a 3D biomimetic culture microenvironment comparable to Matrigel for BEAS-2B cells. They efficiently supports cell proliferation, aggregation, and spheroid formation, and possess great potential to replace Matrigel for the 3D culture of pulmonary epithelial cells.

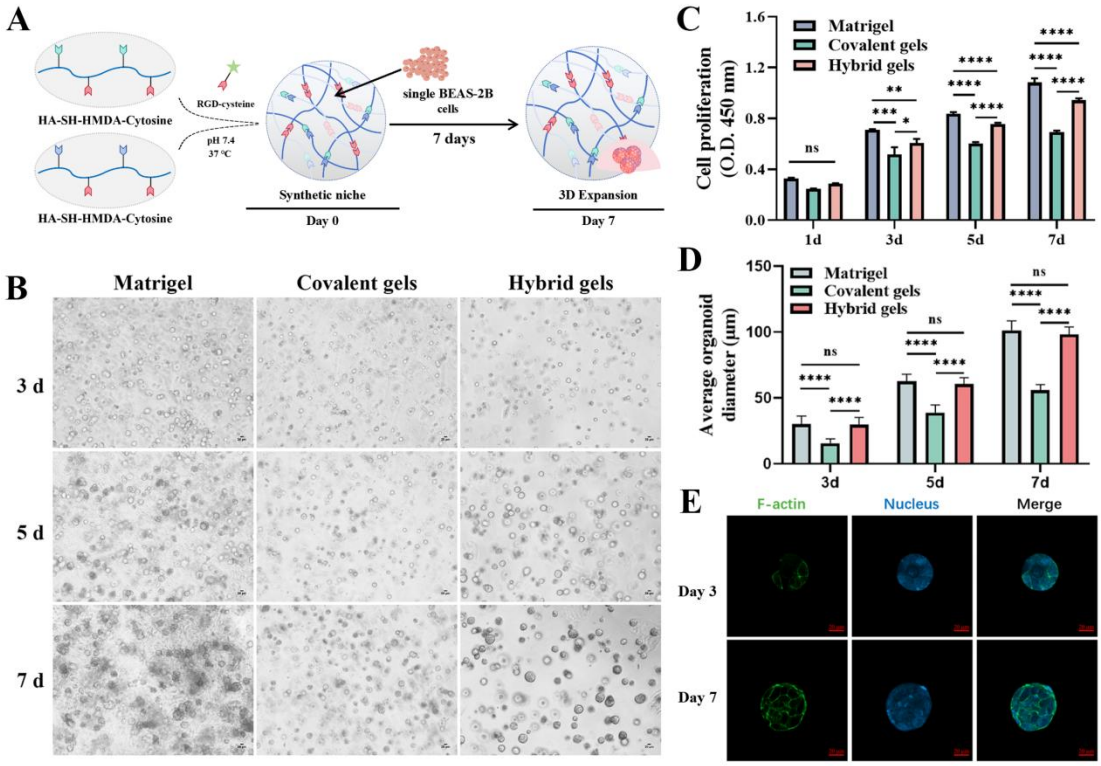


Figure 4. HA-based hydrogels support the construction of 3D BEAS-2B cell spheroid models. (A) Schematic illustration of the experimental procedure for 3D spheroid formation of BEAS-2B cells cultured in synthetic hydrogels and Matrigel. (B) Bright-field microscopic images of BEAS-2B cells cultured in Matrigel, Covalent gels, and Hybrid gels on day 3, day 5, and day 7 (Scale bar: 20 μm). (C) Quantitative analysis of proliferative activity of BEAS-2B cells cultured in different matrices for 1, 3, 5, and 7 days (n=4). (D) Statistical analysis of the average spheroid diameter in Matrigel, Covalent gels, and Hybrid gels on day 3, day 5, and day 7 of culture (n=20). (E) Cytoskeleton staining images of BEAS-2B cells cultured in Hybrid gels on day 3 and day 7 (Scale bar: 25 μm). Data are expressed as mean ± SD. Statistical analysis was performed via two-way ANOVA followed by Dunnett's post-hoc test. *P<0.05, **P<0.01, ***P<0.001, ****P<0.0001; *ns*, no significant difference.

3.5 Construction of a 3D Lung Spheroid Model Based on Hybrid Gel for 1-NP Toxicity Evaluation

Compared with conventional 2D culture, 3D cell culture can better mimic the in vivo tissue morphology, intercellular interactions and microenvironmental barrier effects of the airway epithelium, which more closely approximates the real physiological state. It provides a more physiologically relevant in vitro model for assessing the pulmonary toxicity of environmental pollutants[39]. To evaluate the toxic injury effects of 1-NP on the airway epithelium, a BEAS-2B 3D spheroid model constructed based on Hybrid gel was employed in this study to perform 1-NP exposure experiments with different concentration gradients. Meanwhile, a traditional 2D cell culture system was set as a control to systematically compare the differential characteristics of cellular toxic responses to 1-NP between the two culture modes (Figure 5A). First, a gradient-dose toxicity assay of 1-NP was conducted in the BEAS-2B 3D spheroid model, and the IC_{50} was determined. Bright-field microscopic

observations showed that as the 1-NP concentration increased from 0 μM to 400 μM, the 3D spheroids exhibited evident concentration-dependent damage, accompanied by gradual morphological shrinkage and blurred boundaries. Spheroid structures in the high-concentration group were severely impaired and disintegrated, with a large amount of cell debris observed in the field of view (Supplementary Figure 5A). Cell viability analysis revealed that cell survival rate decreased in a typical sigmoidal dose-dependent manner with elevated 1-NP concentration. Fitting analysis showed that the IC_{50} value of 1-NP in the 3D spheroid model was 56.15 μM, which was significantly higher than 13.80 μM obtained in the 2D culture system (Supplementary Figure 5B, 5C). Based on the above IC_{50} results, 1 μM, 10 μM and 50 μM were selected as the subsequent 1-NP intervention concentrations, corresponding to low-dose environmental exposure, moderate effective concentration and near half-inhibition critical concentration, respectively. This provides a reasonable experimental concentration basis for further exploration of toxicological mechanisms[40].

Morphological observation and Live/Dead staining results showed that the control group (Ctrl) and the low-concentration (1 μM) 1-NP group maintained intact spheroid morphology and clear boundaries without obvious structural damage, and the internal cells remained highly viable. When the 1-NP concentration increased to 10 μM, spheroids began to exhibit structural abnormalities such as shrinkage and marginal damage. In the high-concentration (50 μM) group, most spheroids suffered severe structural collapse with completely blurred boundaries; a large number of dead cells accumulated inside the spheroid cavities, and some spheroids even entirely lost intact structural integrity. These findings further indicated that 1-NP induced obvious concentration-dependent structural damage to BEAS-2B 3D spheroids, and high-dose 1-NP exposure caused severe destruction of spheroid architecture (Figure 5B). Previous studies have demonstrated that 1-NP, as a typical polycyclic aromatic hydrocarbon pollutant, can significantly induce excessive ROS accumulation in pulmonary epithelial cells and subsequently trigger oxidative stress injury_which serves as one of the key mechanisms underlying its cytotoxicity and airway epithelial damage[41]. Therefore, this study further explored the effect of 1-NP exposure on oxidative stress levels in the BEAS-2B 3D spheroid model. The results showed that compared with the Ctrl group, the relative ROS fluorescence intensity in the 10 μM and 50 μM 1-NP groups increased in an obvious dose-dependent manner. Diffuse ROS-specific fluorescence signals were observed in the spheroids of the 50 μM group, indicating that high-concentration 1-NP remarkably activated oxidative stress (Figure 5C, D). In addition, MDA is a representative end product of membrane lipid peroxidation, and its content directly reflects the degree of cellular oxidative damage and lipid peroxidation[42]. MDA detection results were consistent with the ROS trend; MDA levels in both the 10 μM and 50 μM 1-NP groups were significantly higher than those in the Ctrl group (Supplementary Figure 6A). This further confirmed that 1-NP exposure effectively induced lipid peroxidation and exacerbated oxidative stress injury in 3D spheroids, and verified that oxidative stress is a critical mechanism by which 1-NP mediates airway epithelial damage.

To further elucidate the molecular mechanism underlying cell injury induced by 1-NP exposure, the expression patterns of six functionally related genes were detected. Among these, injury biomarker genes (REPS2, H3C12, PRKAA2, and ML167) were significantly upregulated following 1-NP treatment. In contrast, CLDN18 and CDHR4, which are associated with cell membrane structural maintenance and barrier protection, were markedly downregulated, suggesting that 1-NP exposure induced cell membrane structural damage (Supplementary Figure 6B). Once cell membrane integrity is compromised, LDH is released into the extracellular environment. Therefore, LDH release serves as a biomarker for detecting pyroptosis or other types of cell death accompanied by increased membrane permeability[43,44]. LDH release assays showed that the relative LDH release levels were significantly elevated in the 10 μM and 50 μM 1-NP groups, indicating that 1-NP exposure disrupted cell membrane integrity and induced cellular injury (Supplementary Figure 6C).

Tight junctions constitute the most essential physical barrier of the airway epithelium, which effectively seals the gaps between epithelial cells, blocks the transmembrane transport of exogenous pollutants, inflammatory factors, and harmful stimuli, and plays a pivotal role in maintaining respiratory homeostasis and resisting external injury[45]. To investigate the intervention effect of 1-NP on airway epithelial barrier function, Western Blot was used to detect the expression levels of tight junction proteins (Figure 5E, 5F). The results showed that the expression levels of ZO-1, Occludin and Claudin-1 were all downregulated in a dose-dependent manner with increasing 1-NP concentration. Under 50 μM 1-NP treatment, the relative protein expression levels of ZO-1, Occludin and Claudin-1 decreased to 0.49-fold (P<0.05), 0.74-fold (P<0.01) and 0.56-fold (P<0.001) of the Ctrl group, respectively. qPCR detection of gene expression exhibited a highly consistent trend with protein changes (Supplementary Figure 7), further confirming that 1-NP exposure markedly impaired the epithelial barrier integrity of 3D spheroids. In summary, 1-NP exerts significant dose-dependent toxic effects on BEAS-2B 3D spheroids. The underlying mechanisms are closely associated with the induction of excessive ROS accumulation, exacerbation of lipid peroxidation damage, disruption of cell membrane structural homeostasis, and impairment of airway epithelial tight junction barriers. These results demonstrate that the 3D pulmonary epithelial spheroid model constructed based on Hybrid gels possesses good applicability and great application potential in the toxicological evaluation of environmental pollutants and related molecular mechanism research.

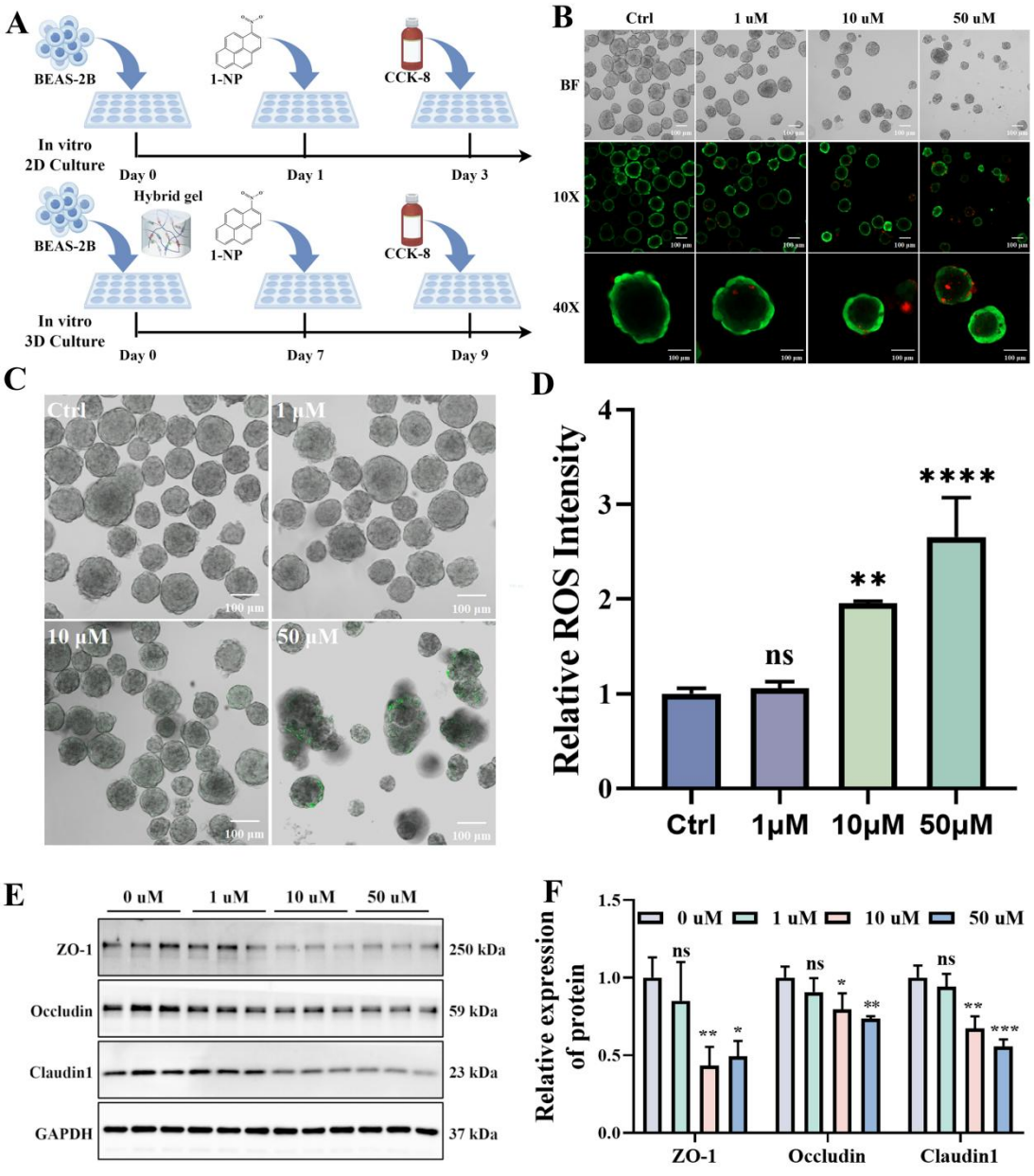


Figure 5 Toxic effects and underlying mechanisms of 1-NP exposure on BEAS-2B 3D spheroids. (A) Schematic overview of the experimental workflow. With conventional 2D cell culture as the control, the BEAS-2B 3D spheroid model constructed by Hybrid gels was employed to systematically evaluate the toxic effects and molecular mechanisms of 1-NP exposure. (B) Representative bright-field images and Live/Dead staining images of BEAS-2B 3D spheroids after treatment with different concentrations of 1-NP. Calcein-AM labeled live cells with green fluorescence, while PI labeled dead cells with red fluorescence (Scale bar: 100 μm). (C, D) Representative fluorescence images and quantitative analysis of intracellular ROS levels after 1-NP treatment with various concentrations of 1-NP. The DCFDA probe was used for specific green fluorescence labeling of ROS (Scale bar: 100 μm). (E, F) Western Blotting detection and grayscale quantitative analysis of tight junction proteins (ZO-1, Occludin, Claudin-1) expression levels in 3D spheroids treated with different concentrations of 1-NP (n=3). Data are expressed as mean ± SD. Statistical analysis was performed via one-way ANOVA followed by Dunnett's post-hoc test. *ns,* no significant difference, *P<0.05, **P<0.01, ***P<0.001, ****P<0.0001vs the

ctrl group.

4. Conclusion

Unlike conventional single-component synthetic hydrogels, the covalent-hydrogen bond dual-network hydrogel fabricated in this study can adaptively accommodate mechanical deformation during cell proliferation and 3D spheroid development, while maintaining a stable network structure and avoiding irreversible structural degradation and collapse. Thus, it exhibits promising application prospects in the field of 3D cell culture. The developed Hybrid gels can precisely mimic the physiological microenvironment of lung tissues and are suitable for the 3D culture of human bronchial epithelial BEAS-2B cell line. Through the synergistic effect of disulfide covalent crosslinking and cytosine-mediated triple hydrogen-bond physical crosslinking, Hybrid gels form a stable dual-network system. With appropriate pore architecture, tunable swelling behavior, and optimized mechanical properties, the hydrogel efficiently supports cell adhesion, proliferation and 3D spheroid formation, showing culture performance comparable to that of Matrigel. When the biomimetic hydrogel-based 3D lung epithelial spheroid model was applied to 1-NP toxicity evaluation, the 3D model exhibited a more physiologically relevant toxic response and a markedly higher IC_{50} value compared with the traditional 2D culture system. Mechanistic investigations revealed that 1-NP induces excessive intracellular ROS accumulation and lipid peroxidation damage, impairs cell membrane integrity, and downregulates the expression of tight junction proteins (ZO-1, Occludin and Claudin-1), thereby disrupting the structural integrity and functional barrier of airway epithelium. In conclusion, the biomimetic HA-based dual-network hydrogel established in this study provides a stable and novel 3D culture model for the in vitro toxicological evaluation of air pollutants. Meanwhile, it offers a feasible in vitro research strategy to reduce and even replace experimental animals in toxicity testing.

CRediT authorship contribution statement

Guojie Zhao: Conceptualization, Methodology, Writing – original draft, Writing – review & editing, Data curation, Funding acquisition. **Conghui Liu:** Writing – original draft, Data curation. **Yanlei Ge:** Writing – review & editing, Funding acquisition, Project administration. **Xuemin Yao:** Formal analysis, Writing – original draft. **Hongjiao Wu:** Supervision, Data curation. **Yishuang Cui:** Validation, Project administration. **Weinan Yao:** Software, Investigation, Supervision, Resources, Project administration. **Junqing Gan:** Supervision, Resources. **Guogui Sun:** Supervision, Writing – review & editing, Resources, Funding acquisition.

Ethics statement

Not applicable

Declaration of competing interest

The authors declare that they have no known competing financial interests or personal relationships that could have appeared to influence the work reported in this paper.

Acknowledgments

This work was supported by the Natural Science Foundation of Hebei Province (Grant No. H2023209083), the Graduate Student Innovation Fund of North China University of Science and Technology (Grant No. CXZZBS2026131), National Natural Science Foundation of China (Grant No. 82472636), the Special Research Projects for Institutions of Higher Education in Hebei Province (Grant No. JZX2024009), Tangshan Municipal Science and Technology Planning Project (Grant No. 25150220E).

Data availability

Data will be made available on request.

References

1. GBD 2021 Risk Factors Collaborators, Global burden and strength of evidence for 88 risk factors in 204 countries and 811 subnational locations, 1990-2021: a systematic analysis for the Global Burden of Disease Study 2021, Lancet 403 (10440) (2024) 2162-2203, https://doi.org/10.1016/S0140-6736(24)00933-4.
2. Y. Niu, R. Chen, H. Kan, Air Pollution, Disease Burden, and Health Economic Loss in China, Adv Exp Med Biol. 1017 (2017) 233-242, https://doi.org/10.1007/978-981-10-5657-4_10.
3. J. Yin, D. Wu, X. Chen, Z. Ye, Q. Li, Organoid for Air Pollution Toxicity Assessment: Advances and Environmental Applicability, Environ Health (Wash) 3 (12) (2025) 1456-1474, https://doi.org/10.1021/envhealth.5c00141.
4. L. Bridgeman, D. Pamies, M. Frangiamone, Human organoids to assess environmental contaminants toxicity and mode of action: towards New Approach Methodologies, J Hazard Mater. 497 (2025) 139562, https://doi.org/10.1016/j.jhazmat.2025.139562.
5. D. Grimm, EPA scraps plan to end all testing in mammals by 2035, Science 383 (6680) (2024) 248, https://doi.org/10.1126/science.ado0969.
6. E. Lee, S. Y. Lee, Y. J.Seong, J. U. Lim, J. Y. Jeong, J. O. Ryu, Y. Hwang, H. Won, S. W. Moon, Y. D. Kim, K. S. Kim, M. H. Moon, S. K. Yoon, Y. E. Sung, M. Kim, B. Ku, D. W Lee, Development of a three-dimensional airway organoid-pillar dish (3D AO-PD) platform for particulate matter-induced airway toxicity analysis, Mater Today Bio. 35 (2025) 102591, https://doi.org/10.1016/j.mtbio.2025.102591.
7. Y. Zhao, N. Yin, R. Yang, F. Faiola, Recent advances in environmental toxicology: Exploring gene editing, organ-on-a-chip, chimeric animals, and in silico models, Food Chem Toxicol. 193 (2024) 115022, https://doi.org/10.1016/j.fct.2024.115022.
8. J. Han, H. Wang, S. Wei, Y. Chen, T. Xu, D. Yin, Perfluorohexanoic acid exhibits more potential for the proliferation, migration, and invasion of triple-negative breast cancer cells under the 3D culture model, J Hazard Mater. 497 (2025) 139551, https://doi.org/10.1016/j.jhazmat.2025.139551.
9. B. W. Huang, J. Q. Gao, Application of 3D cultured multicellular spheroid tumor models in tumor-targeted drug delivery system research, J Control Release 270 (2018) 246-259, https://doi.org/10.1016/j.jconrel.2017.12.005.
10. N. R. Richbourg, A. Rampal, A. Lorenzana, J. F. Flechas-Beltran, S. R. Peyton, The Intersecting Physical Mechanisms That Regulate Cell Viability in 3D Synthetic Hydrogels, Adv Mater. 38 (19) (2026) e21245, https://doi.org/10.1002/adma.202521245.
11. Y. Song, H. Jo, S. Jeong, I. Kim, S. S. Lee, Vascularised Brain Organoids: Engineering Strategies and Neurobiological Applications, Cell Prolif. 59 (3) (2026) e70161, https://doi.org/10.1111/cpr.70161.
12. P. Guerrero-López, A. Martín-Pardillos, J. Bonet-Aleta, A. Mosseri, J. L. Hueso, J. Santamaria, J. M. Garcia-Aznar, 2D versus 3D tumor-on-chip models to study the impact of tumor organization on metabolic patterns in vitro, Sci Rep. 15 (1)

(2025) 19506, https://doi.org/10.1038/s41598-025-03504-8.
13. Y. Chen, Y. Wang, Y. Li, X. Chen, W. Zheng, T. Wang, H. Jia, X. Ma, Design and evaluation of ionically crosslinked multifunctional ELP-SA composite hydrogels for 3D cell culture, Regen Biomater. 12 (2025) rbaf120, https://doi.org/10.1093/rb/rbaf120.
14. T. W. Kao, A. Chiou, K. H. Lin, Y. S. Liu, O. K. Lee, Alteration of 3D Matrix Stiffness Regulates Viscoelasticity of Human Mesenchymal Stem Cells, Int J Mol Sci. 22 (5) (2021) 2441, https://doi.org/0.3390/ijms22052441.
15. E. C. Lloyd, S. Dhakal, S. Amini, R. Alhasan, P. Fratzl, D. R. Tree, S. Morozova, R. J. Hickey, Porous hierarchically ordered hydrogels demonstrating structurally dependent mechanical properties, Nat Commun. 16 (1) (2025) 3792, https://doi.org/10.1038/s41467-025-59171-w.
16. G. Zhao, Y. Ge, Y. Jin, J. Gan, W. Yao, Y. Bi, G. Sun, Research progress and potential of organoids based on biomimetic hydrogel materials, Colloids Surf B Biointerfaces 257 (2026) 115168, https://doi.org/10.1016/j.colsurfb.2025.115168.
17. X. Yang, K. Wu, Y. Liu, Y. Liu, Y. Fu, W. Lin, Z. Mao, X. Wang, H. Guo, Versatile Hyaluronic Acid Hydrogels via pH-Induced Gelation for Multifaceted Cutaneous Wound Healing, Adv Healthc Mater. 15 (7) (2026) e03120, https://doi.org/10.1002/adhm.202503120.
18. Y. Guo, Y. Liu, Z. Zhang, X. Zhang, X. Jin, R. Zhang, G. Chen, L. Zhu, M. Zhu, Biopolymer based Fibrous Aggregate Materials for Diagnosis and Treatment: Design, Manufacturing, and Applications, Adv Mater. 37 (22) (2025) e2414877, https://doi.org/10.1002/adma.202414877.
19. M. K. Eiken, C. J. Childs, L. K. Brastrom, T. Frum, E. M. Plaster, D. W. Ahmed, R. C. Spencer, O. Shachaf, S. Pfeiffer, J. E. Levine, K. D. Alysandratos, D. N. Kotton, J. R. Spence, C. Loebel, Nascent matrix deposition supports alveolar organoid formation from aggregates in synthetic hydrogels, Stem Cell Reports 20 (1) (2025) 102376, https://doi.org/10.1016/j.stemcr.2024.11.006.
20. D. Shugar, J. J. Fox, Spectrophotometric studies of nucleic acid derivatives and related compounds as a function of pH. I. Pyrimidines, Biochim Biophys Acta. 9 (2) (1952) 199-218, https://doi.org/10.1016/0006-3002(52)90147-9.
21. X. Ye, X. Li, Y. Shen, G. Chang, J. Yang, Z. Gu, Self-healing pH-sensitive cytosine- and guanosine-modified hyaluronic acid hydrogels via hydrogen bonding, Polymer 108 (2017) 348-360, https://doi.org/10.1016/j.polymer.2016.11.063.
22. J. Liu, B. Yang, M. Li, J. Li, Y. Wan, Enhanced dual network hydrogels consisting of thiolated chitosan and silk fibroin for cartilage tissue engineering, Carbohydr Polym. 227 (2020) 115335, https://doi.org/10.1016/j.carbpol.2019.115335.
23. A. Chrisnandy, D. Blondel, S. Rezakhani, N. Broguiere, M. P. Lutolf, Synthetic dynamic hydrogels promote degradation-independent in vitro organogenesis, Nat Mater. 21 (4) (2022) 479-487, https://doi.org/10.1038/s41563-021-01136-7.
24. P. Bulpitt, D. Aeschlimann, New strategy for chemical modification of hyaluronic acid: preparation of functionalized derivatives and their use in the formation of

novel biocompatible hydrogels, J Biomed Mater Res. 47 (2) (1999) 152-69, https://doi.org/10.1002/(sici)1097-4636(199911)47:2<152::aid-jbm5>3.0.co;2-i.
25. Y. Yu, B. Yang, D. Tian, J. Liu, A. Yu, Y. Wan, Thiolated hyaluronic acid/silk fibroin dual-network hydrogel incorporated with bioglass nanoparticles for wound healing, Carbohydr Polym. 288 (2022) 119334, https://doi.org/10.1016/j.carbpol.2022.119334.
26. X. Zhang, P. Sun, L. Huangshan, B. H. Hu, P. B. Messersmith, Improved method for synthesis of cysteine modified hyaluronic acid for in situ hydrogel formation, Chem Commun (Camb). 51 (47) (2015) 9662-5, https://doi.org/10.1039/c5cc02367j.
27. J. Ding, R. He, G. Zhou, C. Tang, C. Yin, Multilayered mucoadhesive hydrogel films based on thiolated hyaluronic acid and polyvinylalcohol for insulin delivery, Acta Biomater. 8(10) (2012) 3643-51, https://doi.org/10.1016/j.actbio.2012.06.027.
28. O. Chaudhuri, L. Gu, D. Klumpers, M. Darnell, S. A. Bencherif, J. C. Weaver, N. Huebsch, H. P. Lee, E. Lippens, G. N. Duda, D. J. Mooney, Hydrogels with tunable stress relaxation regulate stem cell fate and activity, Nat Mater. 15(3) (2016) 326-34, https://doi.org/10.1038/nmat4489.
29. M. P. Lutolf, J. A. Hubbell, Synthetic biomaterials as instructive extracellular microenvironments for morphogenesis in tissue engineering, Nat Biotechnol. 23(1) (2005) 47-55, https://doi.org/10.1038/nbt1055.
30. J. Lou, D. J. Mooney, Chemical strategies to engineer hydrogels for cell culture, Nat Rev Chem. 6 (10) (2022) 726-744, https://doi.org/10.1038/s41570-022-00420-7.
31. J. Cui, Y. Gao, C. Lu, H. Wu, Y. Zhang, S. Yin, B. Xue, Y. Cao, H. Lei, Engineering a Thermally Activatable SpyCatcher/SpyTag Protein Ligation for Injectable and In Situ-Forming Hydrogels, Angew Chem Int Ed Engl. 65 (3) (2026) e09477, https://doi.org/10.1002/anie.202509477.
32. Q. Yuan, B. Bao, M. Li, L. Li, X. Zhang, Y. Tang, Bioactive Conjugated Polymer-Based Biodegradable 3D Bionic Scaffolds for Facilitating Bone Defect Repair, Adv Healthc Mater. 13 (7) (2024) e2302818, https://doi.org/10.1002/adhm.202302818.
33. G. Ben Messaoud, S. Aveic, M. Wachendoerfer, H. Fischer, W. Richtering, 3D Printable Gelatin Methacryloyl (GelMA)-Dextran Aqueous Two-Phase System with Tunable Pores Structure and Size Enables Physiological Behavior of Embedded Cells In Vitro, Small 19 (44) (2023) e2208089, https://doi.org/10.1002/smll.202208089.
34. J. Liu, B. Yang, M. Li, J. Li, Y. Wan, Enhanced dual network hydrogels consisting of thiolated chitosan and silk fibroin for cartilage tissue engineering. Carbohydr Polym. 227 (2020) 115335, https://doi.org/10.1016/j.carbpol.2019.115335.
35. L. Hoffmann, M. Duchmann, K. Lazarow, Y. H. Huang, F. Lukas, W. T. Lo,l R. Fei, C. Schmied, M. Lehmann, J. E. Lunn, I. Piazza, J. P. von Kries, V. Haucke, T. Maritzen, Fructose-1,6-bisphosphate couples glycolytic activity to cell adhesion,

Nat Cell Biol. 28 (4) (2026) 739-753, https://doi.org/10.1038/s41556-026-01911-1.
36. S. Damdam, B. Hunnie, P. Jones, M. Hecker, M. Brinkmann, F. C. da Silva Junior, Toxicity assessment of 6PPD-quinone in human lung cells: Insights from BEAS-2B and A549 cell lines, Toxicol In Vitro 110 (2026) 106147, https://doi.org/10.1016/j.tiv.2025.106147.
37. E. Y. Du, H. T. K. Duong, M. A. K. Tolentino, J. L. Houng, P. Suwannakot, K. C. Tjandra, D. H. T. Nguyen, R. D. Tilley, J. Justin Gooding, Ionically crosslinked biohybrid gelatin-based hydrogels for 3D cell culture, Macromol Res. ;33 (7) (2025) 921-931, https://doi.org/10.1007/s13233-025-00380-z.
38. Y. Zhao, J. Gong, H. Liu, H. Huang, W. S. Tan, H. Cai, A chemically defined, mechanically tunable, and bioactive hyaluronic acid/alginate double-network hydrogel for liver cancer organoid construction, Int J Biol Macromol. 282(Pt 2) (2024) 136707, https://doi.org/10.1016/j.ijbiomac.2024.136707.
39. J. van der Vaart, H.Clevers, Airway organoids as models of human disease, J Intern Med. 289 (5) (2021) 604-613, https://doi.org/10.1111/joim.13075.
40. Y. Zhou, C. Li, Y. Chen, Y. Yu, X. Diao, R. Chiu, J. Fang, Y. Shen, J. Wang, L. Zhu, J. Zhou, Z. Cai, Human Airway Organoids and Multimodal Imaging-Based Toxicity Evaluation of 1-Nitropyrene, Environ Sci Technol. 58 (14) (2024) 6083-6092, https://doi.org/10.1021/acs.est.3c07195.
41. J. Wang, M. Pan, Z. Liu, Polycyclic aromatic hydrocarbons bound to microplastics enhance their bioaccumulation and toxicity, inducing mitochondrial damage and apoptosis in lung epithelium. Environ Pollut. 389 (2026) 127385, https://doi.org/10.1016/j.envpol.2025.127385.
42. H. Wang, T. Xu, S. Wei, M. Cao, D. Yin, Assessing the Adverse Impacts of PM2.5 on Olfactory System Using an Air-liquid Interface Culture Model of Primary Olfactory Epithelial Cells, Chem. Res. Chin. Univ. 39 (2023) 415-424, https://doi.org/10.1007/s40242-023-3019-z.
43. C. Wei, W. Jiang, R. Wang, H. Zhong, H. He, X. Gao, S. Zhong, F. Yu, Q. Guo, L. Zhang, L. D. J. Schiffelers, B. Zhou, M. Trepel, F. I. Schmidt, M. Luo, F. Shao, Brain endothelial GSDMD activation mediates inflammatory BBB breakdown, Nature 629 (8013) (2024) 893-900, https://doi.org/10.1038/s41586-024-07314-2.
44. X. Jing, J. H. Park, T. M. Peters, P. S. Thorne, Toxicity of copper oxide nanoparticles in lung epithelial cells exposed at the air-liquid interface compared with in vivo assessment, Toxicol In Vitro 29 (3) (2015) 502-11, https://doi.org/10.1016/j.tiv.2014.12.023.
45. D. Sun, X. Zhao, T. Wiegand, C. Martin-Lemaitre, T. Borianne, L. Kleinschmidt, S. W. Grill, A. A. Hyman, C. Weber, A. Honigmann, Assembly of tight junction belts by ZO1 surface condensation and local actin polymerization, Dev Cell. 60 (8) (2025) 1234-1250.e6, https://doi.org/10.1016/j.devcel.2024.12.012.

Supplementary Files

This is a list of supplementary files associated with this preprint. Click to download.

- Supplementarymaterial.docx